Lawrence Berkeley National Laboratory
LBL Publications

Title
Influence of microstructural heterogeneity on water diffusion in porous clay media: A case study of illite

Permalink
https://escholarship.org/uc/item/7mh3w40r

Journal
Applied Clay Science, 295

ISSN
0169-1317

Authors
Aghlmand, Reza
Dazas, Baptiste
Asaad, Ali
et al.

Publication Date
2027

DOI
10.1016/j.clay.2026.108414

Copyright Information
This work is made available under the terms of a Creative Commons Attribution License, available at https://creativecommons.org/licenses/by/4.0/

Peer reviewed

eScholarship.org Powered by the California Digital Library
University of California

Applied Clay Science 295 (2027) 108414

Contents lists available at ScienceDirect

Applied Clay Science

journal homepage: www.elsevier.com/locate/clay

Research Paper

Influence of microstructural heterogeneity on water diffusion in porous clay media: A case study of illite

Reza Aghlmand [a,*], Baptiste Dazas [a], Ali Asaad [b], Christophe Tournassat [c,d], Fabien Hubert [a], Emmanuel Tertre [a], Eric Ferrage [a]

[a] Université de Poitiers/CNRS, Institut de Chimie des Milieux et Matériaux de Poitiers (IC2MP), Equipe HydrASA, Poitiers, France
[b] Institute of Concrete Structures and Building Materials (IMB/MPA/CMM), Karlsruhe Institute of Technology (KIT), Karlsruhe, Germany
[c] Institut des Sciences de la Terre d'Orléans (ISTO), Université d'Orléans, CNRS, BRGM, OSUC, 45071 Orléans, France
[d] Lawrence Berkeley National Laboratory, Earth & Environmental Sciences Area, Berkeley, CA, USA

ARTICLE INFO

Keywords:
Clay porous media
Water diffusion
Microstructure
CrunchODiTi
Synchrotron 2D-μXRD
Particle orientation

ABSTRACT

Understanding the diffusion of water and solutes in clay-rich materials is critical for several applications, notably radioactive waste disposal. Most of the available experimental data on tracer diffusion in clay porous media are interpreted using only bulk porosity and, to a lesser extent, on particle orientation, implicitly assuming their homogeneity in the sample. Nevertheless, these parameters can be heterogeneously distributed in both natural and laboratory-made clay samples, and a quantitative assessment of their impact on water diffusion is still lacking. To address this gap, synchrotron two-dimensional micro-X-ray diffraction was used to map the microstructural heterogeneity in porosity and clay particle orientation in two laboratory-made illite porous media obtained by compaction in dry conditions or centrifugation in wet conditions. The resulting maps were coupled with the CrunchODiTi reactive transport code to derive the macroscopic water effective diffusion coefficient by accounting for porosity and the orientation tensor of clay particles at each map pixel. The results indicate that heterogeneity in clay particle orientation has a negligible effect on the water effective diffusion coefficients, such that the use of an average value is sufficient. Conversely, pronounced variations in water diffusion values among different porosity heterogeneity patterns (i.e., homogeneous, bedding, and random) demonstrate that the porosity microstructure can either amplify or attenuate diffusion anisotropy associated with the preferred orientation of clay particles. The methodology developed in this work, which integrates microstructural heterogeneity mapping with diffusion calculations, provides a new framework for incorporating the textural properties of clay-rich rocks into the prediction of water and solute transport.

1. Introduction

Owing to their fine particle size, clay minerals develop very low permeability upon compaction while retaining high adsorption and swelling capacities (Bergaya et al., 2006). As a result, these minerals have attracted particular interest in European nuclear waste management as barriers to contaminant migration (Pusch, 1992; Madsen, 1998; Schäfer et al., 2003; Van Loon et al., 2003; Descostes et al., 2004; Pusch, 2006; Appelo et al., 2010; Wang et al., 2022; Maes et al., 2024). Among the various types of clay minerals, Illite Du Puy (IDP; Gabis, 1958) has been widely regarded as an analogous clay model of more complex clay-rich rocks in studies of sorption and diffusion of water and ions (Poinssot et al., 1999; González Sánchez et al., 2008; Glaus et al., 2010; Altmann et al., 2012). Indeed, molecular diffusion is the main transport mechanism of water and solutes in clay porous media with low hydraulic permeability (Martin, 1962; Oscarson, 1994).

The effective diffusion coefficient (D_e) of a tracer (e.g., water, anions, cations) is widely used as a key parameter to express the diffusion of water and ionic species in porous media (Kemper and van Schaik, 1966; Liu et al., 2004; Wu et al., 2012; Jacops et al., 2017). The D_e is often obtained from macroscopic diffusion experiments, particularly Through-Diffusion (TD) experiments (Cho et al., 1993; Van Loon et al., 2004; Tertre et al., 2018; Van Laer et al., 2024). For an inert tracer as water, the interpretation of the measured D_e values ($m^2\ s^{-1}$) is based on the physical parameters such as the bulk porosity (ε) and geometrical factor (Kemper and van Schaik, 1966; Brusseau, 1993; Boving and

* Corresponding author.
E-mail address: reza.aghlmand@univ-poitiers.fr (R. Aghlmand).

https://doi.org/10.1016/j.clay.2026.108414
Received 27 February 2026; Received in revised form 24 September 2026; Accepted 24 September 2026
Available online 8 October 2026
0169-1317/© 2026 The Authors. Published by Elsevier B.V. This is an open access article under the CC BY license (http://creativecommons.org/licenses/by/4.0/).

Grathwohl, 2001), as follows:

$$D_e/D_0 = \varepsilon/G \quad (1)$$

where ε (dimensionless) is the accessible porosity for the tracer (i.e., equal to the total porosity in the case of water), D_0 ($m^2\ s^{-1}$) is the self-diffusion coefficient of the tracer in bulk water, and G (dimensionless) is the geometrical factor describing the impact of pore network geometry.

Recently, efforts have been made to refine the interpretation of water diffusion in pure clay systems by accounting for the influence of clay particle orientation (i.e., $\langle P_2 \rangle$ order parameter) in the geometrical factor G (Dabat et al., 2019, 2020; Asaad et al., 2021; Ferrage et al., 2023). To do so, those authors performed Brownian dynamics simulations of water diffusion within three-dimensional virtual granular porous media mimicking the particle shape distributions of illite, kaolinite and vermiculite. By accurately accounting for clay particle orientation and compaction properties within these micrometer-size virtual porous media, the authors were able to correctly reproduce experimental water tracer diffusion data obtained from centimeter-scale samples. In addition, a modified Archie-like model accounting for the distinct roles of both ε and $\langle P_2 \rangle$ parameters was proposed (Ferrage et al., 2023). These findings showed that a correct description of the solid microstructure in pure clay samples can lead to an implicit description of the pore network anisotropy and connectivity that control the overall water diffusion process (Tyagi et al., 2013; Ferrage et al., 2023). For monophasic clay materials, such confrontation relies, however, on the assumption that porosity and/or orientation of clay particles are homogenous throughout the sample and correspond to bulk values. This assumption of sample homogeneity requires an extensive study on the potential influence of microstructural heterogeneity on D_e values, as different preparation methods may lead to a certain degree of heterogeneity, which in turn can impact the measured diffusion coefficients (e.g., compaction in dry conditions or centrifugation in wet conditions; Dabat et al., 2020; Asaad et al., 2021).

As far as natural polyphasic rocks are concerned, the expected heterogeneity in the distribution of ε and $\langle P_2 \rangle$ parameters is likely to be further enhanced (Koltermann and Gorelick, 1996; Huysmans and Dassargues, 2006; Hemes et al., 2013; Pardoen et al., 2020; Yuan et al., 2022). For instance, Robinet et al. (2012) linked water diffusion anisotropy to the organization and elongation of carbonate and tectosilicate grains (i.e., leading to heterogeneity in porosity distribution), thus demonstrating the importance of the microstructure on D_e values in a natural Callovo-Oxfordian clay sample.

In this study, the quantitative effect of heterogeneity in the distribution of porosity and particle orientation on water diffusion is investigated in detail for IDP porous media. For this purpose, ε and $\langle P_2 \rangle$ maps are first obtained using the synchrotron bidimensional micro-X-Ray Diffraction (2D-μXRD) technique on two differently prepared IDP porous media (i.e., compaction and centrifugation) to reveal the real microstructural heterogeneity of these samples. Using the CrunchODiTi reactive transport code (Sarsenbayev et al., 2025), a comparison is made between the experimental D_e values for water obtained for these samples by Asaad (2021) and the calculated ones by considering either the real microstructural heterogeneity of the samples or only the averaged ε and $\langle P_2 \rangle$ parameters. Finally, the roles played by ε and $\langle P_2 \rangle$ microstructures on water diffusion are extended to various types of heterogeneity patterns to quantitatively assess their influence on measured D_e values.

2. Materials and methods

2.1. Preparation of illite samples

Illite material used in this work is the Na-saturated, $0.1 - 0.2$ μm size fraction of illite du Puy (Puy-en-Velay, Haute-Loire, France). The preparation and characterization of this size fraction are detailed in Asaad et al. (2022).

The two porous media prepared by Asaad (2021) for measuring water effective diffusion coefficients using compaction or centrifugation methods were considered in the present study. These two samples have a similar porosity value ($\varepsilon \sim 0.36$) but different $\langle P_2 \rangle$ values. These samples were then replicated for microstructural mapping using 2D-μXRD technique. For this purpose, the samples were first dried by immersion in slush nitrogen before lyophilization and resin induration, at a constant volume, using the protocol described in detail by Asaad et al. (2021). The dimensions of the resin-coated samples were 6.4 mm in diameter and 10 mm in height. Finally, the samples were longitudinally sectioned through their center using a water-cooled circular saw and then reduced in thickness (730 and 1180 μm thick for the compacted and centrifuged samples, respectively) using 15 μm pre-polishing paper for 2D-μXRD analysis.

2.2. Synchrotron 2D-μXRD mapping

2.2.1. Data acquisition

The experiment was performed at the CRISTAL beamline located at the SOLEIL synchrotron (Saint-Aubin, France), using a configuration similar to that employed in the study of Geoffroy et al. (2022). Briefly, the 2D-μXRD mapping measurements were performed in transmission mode using a Si(111) double crystal monochromator with a wavelength (λ) of 0.66894 Å and an X-ray Pixel Array Detector (XPAD 3.2) positioned at a distance of 375 mm from the sample. A counting time of 0.4 s per point (with a pixel size of 76.85 μm) was used to automatically acquire 2D-μXRD maps of the IDP samples. The overall dimensions of the map were $L_{xy} = 36$ px and $L_z = 78$ px for both samples (with the z-direction parallel to the compaction or centrifugation pressure), with L_{xy} taken between the center and the edge of the cylindrical sample. To derive porosity values for each pixel, a transmission map was also recorded with a counting time of 1.5 ms per point. This was accomplished using a Basler camera to capture the total transmitted signal through the resin-embedded thin section and through air (without sample), in order to obtain the transmission ratio T for each pixel.

2.2.2. Data treatment

All data processing was performed using the LamelODF software (Dazas et al., 2026) to manage all steps required for data treatment, data correction as well as subsequent analysis (Geoffroy et al., 2022). The analysis of each individual 2D-μXRD pattern is illustrated in Fig. 1 for a single pixel of the map of the centrifuged IDP sample. As seen in Fig. 1a, the (001) reflection ring of illite along the azimuthal detector angle τ is highly anisotropic with a deviation angle Δ between the principal orientation of clay particles and the detector reference. In Fig. 1b, the integrated intensity values $I(\tau)$ for IDP samples (between 6.68 and 10.41 Å) are extracted over 360 degrees of the τ angular range on the detector (Fig. 1a) with an 8° angular step. The generalized orientation distribution function (ODF) introduced by Dabat et al. (2019) was applied in an automated fitting process of experimental $I(\tau)$ data of each pixel. This function takes the following form:

$$I(\tau) = k' \exp\left[\lambda_2 P_2(\cos(\theta + \Delta)) + 0.005(\lambda_2)^5 P_4(\cos(\theta + \Delta))\right] \quad (2)$$

where λ_2 and k' represent the ODF spreading parameter and a normalization constant, respectively. The θ stands for the angle between the normal of the clay particle and the principal axis of the orientation tensor. The $P_2(\cos\theta)$ and $P_4(\cos\theta)$ are the second- and fourth-order Legendre polynomials, respectively, expressed as:

$$P_2(\cos\theta) = \frac{1}{2}\left(3\cos^2\theta - 1\right) \quad (3)$$

$$P_4(\cos\theta) = \frac{1}{8}\left(35\cos^4\theta - 30\cos^2\theta + 3\right) \quad (4)$$

The ODF $f(\theta)$ can be derived from Eq. (2) by considering the

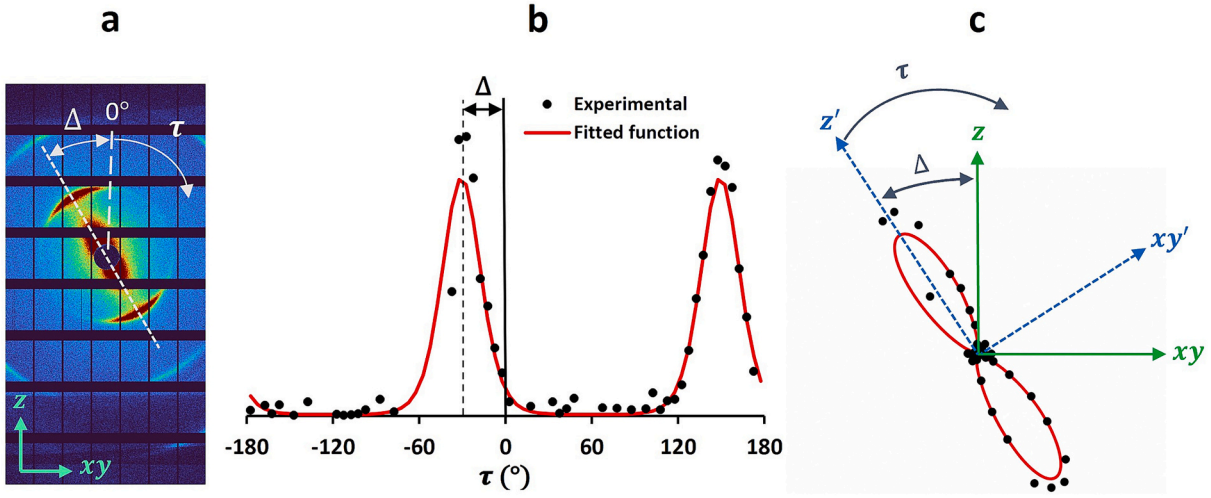


Fig. 1. Extraction of clay particle orientation from 2D-μXRD technique. (a) Individual 2D-μXRD pattern showing the intensity distribution $I(\tau)$ on the (001) diffraction ring (dark red areas) for the centrifuged IDP sample. The azimuthal angle τ and the detector reference are also shown. (b) Comparison between the experimental $I(\tau)$ data (solid circle) and the fitted function (solid red line) to determine the deviation angle Δ of the orientation tensor and the degree of particles orientation $\langle P_2 \rangle$. (c) Orientation tensor of particles derived from the 2D-μXRD pattern in polar coordinates and its relation with *xyz* detector reference. (For interpretation of the references to colour in this figure legend, the reader is referred to the web version of this article.)

following relation:

$$I(\tau) = k' f(\theta + \Delta) \tag{5}$$

Based on the fitted ODF in Fig. 1b and associated constraints that define the $f(\theta)$ function (Dabat et al., 2019), the degree of particle orientation, i.e., $\langle P_2 \rangle$ parameter, can be calculated as follows:

$$\langle P_2 \rangle = \int_0^{\pi} P_2(\cos\theta)\, f(\theta)\, \sin(\theta)\, d\theta \tag{6}$$

with $\langle P_2 \rangle = 0$ for isotropic orientation and $\langle P_2 \rangle = 1$ for perfectly oriented clay particles.

In Fig. 1c, the fitted $I(\tau)$ function is plotted in polar coordinates to represent the anisotropic orientation tensor of particles derived from the 2D-μXRD pattern, as shown in Fig. 1a.

This data processing enables the determination of $\langle P_2 \rangle$ and Δ parameters for each pixel, thereby characterizing the orientation of the particles with respect to the map coordinates. Regarding porosity, the ε value for each pixel was determined by combining the X-ray transmission measurements with a theoretical calculation of attenuation for an illite crystal. The attenuation contribution of the embedding resin to the transmission ratio T was considered negligible (~ 7% attenuation for 1000 μm of pure resin at the experimental energy). For illite crystal, the theoretical linear attenuation coefficient μ (cm^{-1}) was calculated from the chemical formula of illite using the NIST photon attenuation databases (Hubbell and Seltzer, 1995) as $\mu = \mu_m \times \rho$, where μ_m is the calculated mass attenuation coefficient (3.0697 $cm^2\ g^{-1}$) derived from the elemental composition of the mineral, and ρ is the mineral density (i.e., 2.83 g cm^{-3}; Asaad et al., 2022). Assuming that the transmission is governed solely by the mineral matter, the theoretical thickness $d_{theo.}$ at the origin of the measured T values was calculated using the Beer-Lambert law $T = \exp(-\mu\, d_{theo.})$, which can be rearranged to $d_{theo.} = -\ln(T)/\mu$. The porosity value ε at each pixel was then determined from the difference between the actual sample thickness ($d_{act.} = 730$ or 1180 μm for the compacted or centrifuged sample, respectively) and the theoretical thickness $d_{theo.}$ as follows:

$$\varepsilon = 1 - (d_{theo.}/d_{act.}) \tag{7}$$

2.3. Two-dimensional reactive transport modeling

The reactive transport code CrunchODiTi (for Off-Diagonal Terms integration) was used for the calculation of effective water diffusion coefficients $D_{e\overline{xy}}$ and D_{ez} along the $\overline{xy}$- and *z*-directions of the two-dimensional (2D) map, respectively. This code is an evolving branch of the established CrunchFlow code (Steefel et al., 2015) and of its CrunchClay flavor. It offers various benefits, including the simplicity of incorporating effective diffusion coefficients in multiple directions and its specialized design for reactive transport in clay materials (Tournassat and Steefel, 2021; Tournassat et al., 2023; Fox et al., 2024; Sarsenbayev et al., 2025).

For both $\overline{xy}$- and *z*-directions, the CrunchODiTi simulations were carried out by assigning a set of ε, $G_{\overline{xy}}$, and G_z values to each pixel, where $G_{\overline{xy}}$ and G_z correspond to the geometrical factors in the *xyz* frame of the 2D map. These geometrical factors were first calculated for each pixel in the referential frame of the orientation tensor through the extended Archie relations proposed by Ferrage et al. (2023) for different types of clay minerals (i.e., kaolinite, illite, vermiculite) as:

$$G'_{\overline{xy}} = \varepsilon \Big/ \left(\left(0.48\, \varepsilon^{1.2} - 0.272\, \langle P_2 \rangle\, \varepsilon\right) e^{1.55\, \langle P_2 \rangle} \right) \tag{8}$$

$$G'_z = \varepsilon \Big/ \left(0.48\, \varepsilon^{1.2} - 0.272\, \langle P_2 \rangle\, \varepsilon\right) \tag{9}$$

Then, considering that the orientation tensor of particles can be rotated regarding the *xyz* referential frame of the 2D map by an angle Δ (see section 2.2.2 and Fig. 1c), a rotation matrix calculation was applied to retrieve the final geometrical factors in the referential frame:

$$G_{\overline{xy}} = G'_{\overline{xy}} \cos^2(\Delta) + G'_z \sin^2(\Delta) \tag{10}$$

$$G_z = G'_{\overline{xy}} \sin^2(\Delta) + G'_z \cos^2(\Delta) \tag{11}$$

The amount of tracer in the upstream and downstream reservoirs was set to $C_{0,Up} = 1 \times 10^{-3}$ mol kg^{-1} and $C_{0,Down} = 1 \times 10^{-33}$ mol kg^{-1}, respectively. The default value of D_0 was set to $2.3 \times 10^{-9}\ m^2\ s^{-1}$ (Mills, 1973; Holz et al., 2000). For each map, two simulations were carried out along the $\overline{xy}$- and *z*-directions, respectively.

2.4. Up-scaling of diffusion parameters at the sample scale

The time evolution of tracer concentration in the downstream reservoir (i.e., the breakthrough curve) was used to determine the average values of $D_{e\overline{xy}}$ and D_{ez} coefficients, which apply at the sample scale, through Fick's second law:

$$\frac{\partial C}{\partial t} = \frac{D_e}{\alpha}\frac{\partial^2 C}{\partial x^2} \quad (12)$$

with C the aqueous concentration (mol m^{-3}), t the time (s), D_e the effective diffusion coefficient (m^2 s^{-1}), and α the rock capacity factor (dimensionless). For our inert tracer, α corresponds to the porosity ε in the sample. The effective diffusion coefficient D_e is related to the porosity, self-diffusion coefficient in bulk water (i.e., D_0) and G by Eq. (1). The tracer concentration breakthrough curves obtained with the 2D reactive transport modeling approach were fitted with an analytical

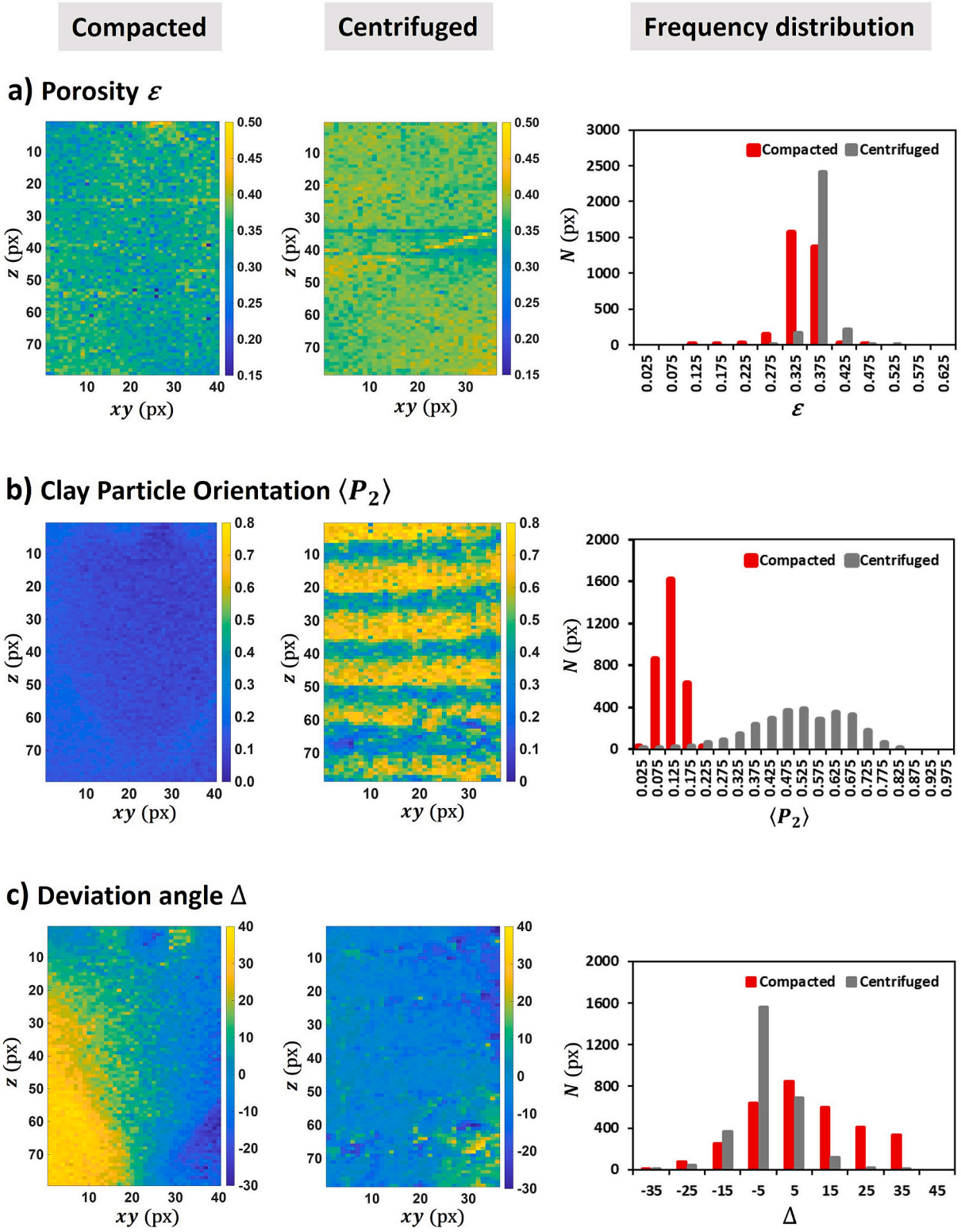


Fig. 2. Colour-code mapping (left and center) and frequency distribution (right) of different parameters, including (a) porosity (ε), (b) preferred orientation of clay particle $\langle P_2 \rangle$ parameter, and (c) deviation angle of the particle orientation tensor (Δ) for both compacted and centrifuged IDP samples based on synchrotron depth-averaged 2D-μXRD analyses. The map pixel size is 76.85 μm.

solution of Fick's second law using the following initial and boundary conditions: $C(x, t = 0) = 0$, $C(x = L, t) = 0$, and $C(x = 0, t > 0) = C_{0,up}$, where L is the thickness of the sample. These calculations were carried out using the CrunchEase package (Tournassat et al., 2023; and references therein).

3. Results and discussion

3.1. 2D-μXRD mapping of IDP samples

The obtained mapping of ε, $\langle P_2 \rangle$, and Δ values from the 2D-μXRD synchrotron scans for both compacted and centrifuged IDP samples are presented in Fig. 2 as colour-coded maps and frequency distributions. As shown in Fig. 2a, the porosity distribution is almost homogeneous for both samples, with a narrow range of porosity values, leading to an average ε values of 0.34 (with 0.06 as 2σ standard deviation) for the compacted IDP and 0.38 (with $2\sigma = 0.04$) for the centrifuged IDP samples (Fig. 2a). This indicates that the sample preparation method has little impact on the heterogeneity in porosity values.

Conversely, the different preparation methods of IDP samples result in a significant difference in $\langle P_2 \rangle$ distribution frequency (Fig. 2b). In the compacted sample, the distribution frequency of $\langle P_2 \rangle$ is almost homogeneous, within the range of 0.05 to 0.20, and an average value of $\overline{\langle P_2 \rangle} = 0.12$ (with 0.06 as 2σ standard deviation). The situation differs for the centrifuged sample, as the 2D-μXRD map exhibits a repetitive pattern along the z-direction. Each pattern in Fig. 2b consists of a yellow and blue area indicating high and low $\langle P_2 \rangle$ values, respectively, which corresponds to one centrifuge cycle leading to the formation of a bedding. This bedding pattern, likely resulting from the segregation of particle sizes during centrifugation and contrasted orientation properties, logically leads to a wide frequency distribution of $\langle P_2 \rangle$ values, ranging between 0.3 and 0.7, with an average $\overline{\langle P_2 \rangle}$ value of 0.52 (with $2\sigma = 0.28$).

Analysis of the Δ parameter indicates that the frequency distributions are centered close to zero for both IDP samples. However, the different preparations lead to contrasted distribution widths (Fig. 2c). In the centrifuged sample, the distribution is rather narrow, indicating that the pressure induced by centrifugation is almost homogeneous and aligned with the z-axis. In the compacted IDP sample, the high and low Δ values on the bottom part of the map can be attributed to the compaction process (Fig. 2c). This leads to the rotation of the particle orientation tensor, aligning alongside with the local pressure axes, which may differ between the center and border of the sample (Fig. 2c). This interpretation is consistent with the slight increase of $\langle P_2 \rangle$ values in these regions (Fig. 2b).

3.2. Comparison between simulated and experimental effective diffusion coefficients

Based on the ε, $\langle P_2 \rangle$, and Δ maps from 2D-μXRD technique (Fig. 2), the overall effective water diffusion coefficients (i.e., $D_{e\overline{xy}}$ and D_{ez}) are calculated using the CrunchODiTi code along the $\overline{xy}$- and z-directions of the maps, according to Eqs. (1), (10), and (11). The results are reported in Table 1, together with the same calculations considering only the average values of ε, $\langle P_2 \rangle$, and Δ for all pixels (i.e., homogeneous microstructure). For both IDP samples, the simulated effective diffusion coefficients are almost identical between the homogeneous and synchrotron-derived heterogeneous maps (less than 5% difference on $D_{e\overline{xy}}$ and D_{ez} values; Table 1). Similarly, the diffusion anisotropy ratio $D_{e\overline{xy}}/D_{ez}$ is almost equal for both types of microstructures. Such a finding indicates that, given the observed degree of heterogeneity of the samples for the ε, $\langle P_2 \rangle$, and Δ parameters, the influence of microstructural heterogeneity on the water diffusion coefficients is negligible, and that only the average values are sufficient (Fig. 2; Table 1). It should be noted that the highly heterogeneous distribution of $\langle P_2 \rangle$ values for the centrifuged sample has surprisingly little impact on the calculated diffusion values (Fig. 2b; Table 1).

The simulated D_{ez} values can be compared with those reported by Asaad (2021) for the two IDP samples, which were obtained from TD experiments (Table 1). The difference in D_{ez} values between the two IDP samples with a similar porosity value is fully consistent with the increase in $\langle P_2 \rangle$ for the centrifuged sample and thus further demonstrates the influence of preferred orientation of clay particles on water dynamics (Dabat et al., 2020; Asaad et al., 2021; Ferrage et al., 2023). However, the overall D_{ez} values in the simulations are noticeably higher than the experimental data of Asaad (2021). Two factors may account for this discrepancy. First, the simulated D_{ez} values here, using Eqs. (1) and (9), are based on the extended Archie model proposed by Ferrage et al. (2023). These authors reported a better agreement between the experimental and calculated effective diffusion coefficients for kaolinite compared to IDP, for which simulations led to higher D_{ez} values. This difference was attributed to the lack of consideration of the mobility reduction of water molecules at the interface with the external charged surfaces of illite in the simulations. Second, the determination of the experimental D_e values is subject to biases related to the geometry of the TD diffusion cell. For instance, Glaus et al. (2008) demonstrated the necessity of considering the impact of the filters used to homogenize the solution in data analysis. Furthermore, Fox et al. (2024) and Tournassat et al. (2023) reported a significant effect of the O-rings between the clay sample and the sample holder. More recently, Désert et al. (2026) confirmed the contributions of filters and O-rings on the D_e value for the same IDP porous media. In addition, these authors showed that the localized solution injection canals of the sample holder play a role in limiting water diffusion as well as the interface with the sample. If these factors are not properly considered in the data analysis, the real D_e value can be up to ~ 25% higher than the measured one (Désert et al., 2026). As far as the study by Asaad (2021) is concerned, the author accounted for the filter effect, but not for the other contributing factors, which likely led to an underestimation of the D_{ez} value. The D_{ez} value reported by Désert et al. (2026) using in-situ neutron tomography imaging of water diffusion during TD experiment is found to be more compatible with the simulated D_{ez} value in the present study. Interestingly, Désert et al. (2026) showed that the actual D_{ez} value of 2.63×10^{-10} m^2 s^{-1} decreased to 2.08×10^{-10} m^2 s^{-1} without correction of the diffusion cell geometry, the latter value being consistent with the upper D_{ez} limit reported by Asaad (2021) (Table 1). Considering the two above-mentioned influential factors on the overestimation of D_e in simulations and its underestimation in experiments, the discrepancies between the

Table 1
Simulated effective water diffusion coefficients D_e ($\times 10^{-10}$ m^2 s^{-1}) using ε, $\langle P_2 \rangle$, and Δ parameter distribution from 2D-μXRD maps as well as using only the averaged values (homogeneous microstructure). The simulated D_e values are compared with the experimental through-diffusion (TD) data obtained by (Asaad, 2021) for the same IDP samples as well as with other data from a similar compacted IDP sample (Désert et al., 2026).

Sample type	Simulated (2D-μXRD)			Simulated (homogeneous)			Experimental (TD)	
	$D_{e\overline{xy}}$	D_{ez}	$D_{e\overline{xy}}/D_{ez}$	$D_{e\overline{xy}}$	D_{ez}	$D_{e\overline{xy}}/D_{ez}$	D_{ez} [a]	D_{ez} [b] ($\bar{\varepsilon} = 0.38$)
Compacted	3.37	2.90	1.16	3.40	2.84	1.19	1.70 (1.31–2.08)	2.63
Centrifuged	4.91	2.24	2.19	5.08	2.27	2.24	1.05 (0.88–1.31)	–

Data from [a] (Asaad, 2021) and [b] (Désert et al., 2026), assuming $D_0 = 2.3 \times 10^{-9}$ m^2 s^{-1}.

simulated and experimental D_{ez} values in Table 1 can be moderated.

3.3. Influence of microstructural heterogeneity on the effective water diffusion coefficients

Based on the above comparison of D_e values between the homogeneous and heterogenous distributions of ε, $\langle P_2 \rangle$, and Δ parameters for the two IDP samples (Table 1), it can be tentatively concluded that the influence of heterogeneous microstructure is not required for interpreting water diffusion properties. However, the two samples display a narrow porosity distribution, thus hampering the investigation of the role played by ε heterogeneity on the overall D_e value (Fig. 2a). Furthermore, although the observed bedding in $\langle P_2 \rangle$ values for the centrifuged sample is found to have little impact on the overall D_e value (Fig. 2b; Table 1), one may question if other types of patterns could lead to an increased influence of this parameter on the dynamic properties of water. In the following, the theoretical microstructural maps of the same pixel dimensions as in Fig. 2 are generated to independently investigate the role played by heterogeneous organizations of $\langle P_2 \rangle$ or ε on the overall water dynamics in illite porous media.

3.3.1. Influence of heterogeneity in $\langle P_2 \rangle$ microstructure

The centrifuged IDP sample discussed in the previous sections was considered in order to investigate the impact of heterogeneity in $\langle P_2 \rangle$ microstructure on water dynamics. By integrating the $\langle P_2 \rangle$ values along the $\overline{xy}$-direction and examining the evolution of obtained values in the z-direction (i.e., $\langle P_2 \rangle_z$; Fig. 3), the observed bedding pattern can be approached by a simple sinusoidal function in the general form as:

$$\langle P_2 \rangle_z = A \sin(\omega z + \varphi) + \overline{\langle P_2 \rangle} \tag{13}$$

with $|A|$ the amplitude, ω the pulse, φ the phase shift in the z-direction, and $\overline{\langle P_2 \rangle}$ the vertical shift corresponding to the mean $\langle P_2 \rangle$ value of the entire sample (i.e., $\overline{\langle P_2 \rangle} = 0.52$). The fit of experimental $\langle P_2 \rangle_z$ profile in Fig. 3 led to the following sinusoidal function as: $\langle P_2 \rangle_z = 0.15 \sin(0.44\, z + 0.5) + 0.52$, with z in pixels. Different microstructures can be computed according to the general sinusoidal function in Eq. (13). The $\langle P_2 \rangle$ homogeneous organization can be defined as $A = 0$, and an increase in the A parameter enhances the contrast range (referred to as $CR_{\langle P_2 \rangle}$) between the maximum and minimum $\langle P_2 \rangle$ values in each bedding (i.e., $CR_{\langle P_2 \rangle} = 2A$). Finally, a change in the ω parameter modifies the number of $\langle P_2 \rangle$ beddings (referred to as $n_{\langle P_2 \rangle}$) in the map as $n_{\langle P_2 \rangle} = \omega L_z / 2\pi$, with L_z the z-dimension of the map (px).

In Fig. 4a, the influence of $n_{\langle P_2 \rangle}$ on D_e values is first investigated for a $CR_{\langle P_2 \rangle}$ value of 0.3, the same as that of the centrifuged IDP sample

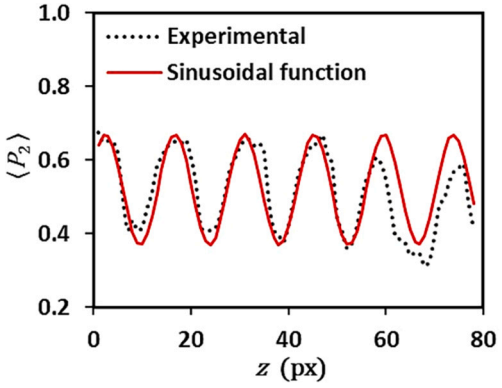


Fig. 3. Evolution of the experimental $\langle P_2 \rangle$ values along the z-axis for the centrifuged sample extracted from Fig. 2b. The experimental profile (dotted line) is fitted by a sinusoidal function (red line). (For interpretation of the references to colour in this figure legend, the reader is referred to the web version of this article.)

(Fig. 3). The mean porosity value is 0.38 and $\overline{\langle P_2 \rangle}$ is 0.52 for the entire set of calculations. Five individual maps were generated for different numbers $n_{\langle P_2 \rangle}$ of beddings, ranging from 1 to 16 (i.e., 1, 2, 4, 8, and 16; Fig. 4a). The overall $D_{e\overline{xy}}$ and D_{ez} values computed with CrunchODiTi reactive transport modeling reveal that increasing the number of $\langle P_2 \rangle$ beddings from 1 to 16 does not influence the overall water mobility. This can be explained by the repetition of the same textural pattern with no impact on the minimum and maximum $\langle P_2 \rangle$ values when $n_{\langle P_2 \rangle}$ is increased, thus leading to a similar effect on the geometrical factor in both the $\overline{xy}$- and z-directions. Furthermore, as shown in Fig. 4a, the $D_{e\overline{xy}}$ and D_{ez} values are very close to the homogeneous case (i.e., $CR_{\langle P_2 \rangle} = n_{\langle P_2 \rangle} = 0$), which confirms the observed limited impact of $\langle P_2 \rangle$ heterogeneity on the overall water diffusion coefficients (see section 3.2 and Table 1). The modeling exercise was repeated for $CR_{\langle P_2 \rangle} = 0.9$ in order to assess whether drastically increasing the contrast range value to its maximum would produce the same results. As shown in Fig. 4a for $CR_{\langle P_2 \rangle} = 0.9$, the number of $\langle P_2 \rangle$ beddings for $n_{\langle P_2 \rangle} \geq 1$ does not lead to different water diffusion results in spite of the fact that the calculated D_e values slightly decrease in both $\overline{xy}$- and z-directions.

The impact of the $CR_{\langle P_2 \rangle}$ parameter on D_e values is best revealed in Fig. 4b, where the bedding number is held constant at $n = 5.5$ (i.e., same as for the centrifuged sample; Figs. 2b and 3). The simulations indeed show a slight decrease in D_e values (i.e., $\sim$ 10% and $\sim$ 5% for D_{ez} and $D_{e\overline{xy}}$, respectively) for the highest $CR_{\langle P_2 \rangle}$ value. This marginal impact of $CR_{\langle P_2 \rangle}$ can be interpreted by the high $\langle P_2 \rangle$ pixels of the map that limit the diffusion process of water in the z-direction, thereby slightly increasing the overall tortuosity in the sample. This simulation set is also compared with a fully random pattern (see map inserts in Fig. 4b), which was obtained by considering the bedding pattern and changing the pixel positions randomly in the map. The perfect match between the bedding and the random patterns for a given $CR_{\langle P_2 \rangle}$ value indicates that, although the contrast between the minimum and maximum $\langle P_2 \rangle$ values can lead to a limited D_e evolution (Fig. 4b), the microstructural heterogeneity pattern (i.e., bedding vs. random) has no influence.

Comparing the calculated D_e values obtained for the different $\langle P_2 \rangle$ microstructures (i.e., homogeneous, bedding, and random) reveals marginal differences (i.e., < 10%). As far as the centrifuged IDP sample is concerned, these results further confirm the almost identical D_e values when considering either the actual 2D-μXRD maps of $\langle P_2 \rangle$ or only the averaged $\langle P_2 \rangle$ value (i.e., homogeneous microstructure). Despite the fact that the bulk $\langle P_2 \rangle$ parameter remains of prime importance for the interpretation of TD results (Ferrage et al., 2023), a detailed description of its spatial heterogeneity within the sample is thus not necessary. As a result, considering only a mean $\langle P_2 \rangle$ value is sufficient to determine overall D_e values, thus validating the homogeneous assumption made in previous studies (Dabat et al., 2020; Asaad et al., 2021; Porion et al., 2021).

3.3.2. Influence of heterogeneity in ε microstructure

Investigation of the impact of heterogeneity in porosity microstructure (i.e., homogeneous, bedding or random pattern) is carried out using the same methodology as done above for $\langle P_2 \rangle$ parameter (Fig. 5). The bedding pattern for ε is defined as:

$$\varepsilon_z = A \sin(\omega z + \varphi) + \overline{\varepsilon} \tag{14}$$

Simulations were conducted for two degrees of particle orientation (i.e., $\overline{\langle P_2 \rangle} = 0.00$ and 0.52) and a mean porosity value $\overline{\varepsilon} = 0.38$ (Fig. 5). The simulation results are again independent of the number of beddings in both the xy- and z-directions (Fig. 5a). For $\overline{\langle P_2 \rangle} = 0$ and a contrast range in porosity values $CR_\varepsilon = 0.3$, a slight variation in diffusion values is found when comparing the bedding pattern with the homogeneous organization (i.e., almost no change in $D_{e\overline{xy}}$ and about 10% decrease in D_{ez} values). Increasing the CR_ε parameter up to 0.7 causes a significant change in D_e values (i.e., $\sim$ 80% decrease in D_{ez} value and $\sim$ 10%

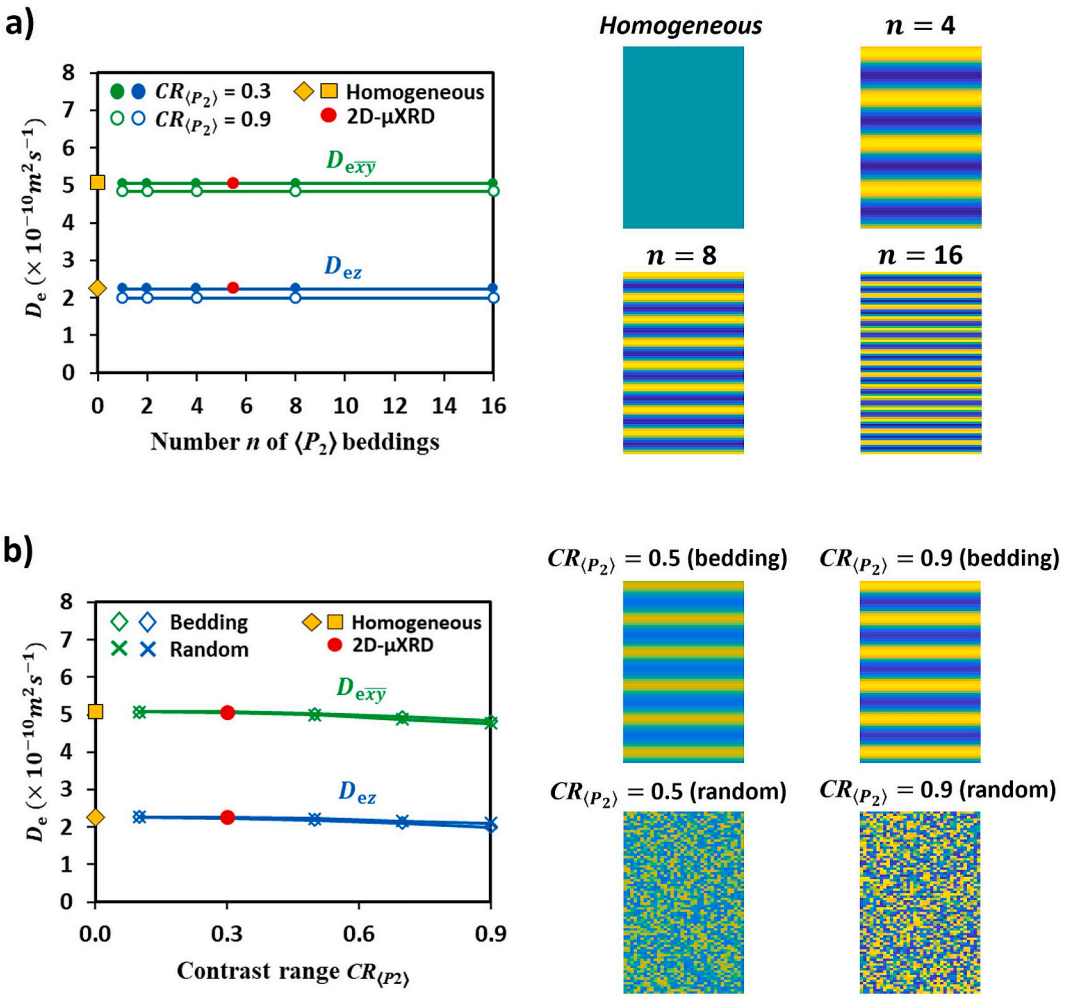


Fig. 4. Influence of the microstructure in preferred orientation of clay particles (parameter $\langle P_2 \rangle$) on the calculated water effective diffusion coefficient (D_e) for a mean porosity $\bar{\varepsilon} = 0.38$ and a mean $\overline{\langle P_2 \rangle}$ value of 0.52. (a) Evolution of D_e values with the number $n_{\langle P_2 \rangle}$ of beddings for two contrast ranges, i.e., $CR_{\langle P_2 \rangle} = 0.3$ (solid circles) and $CR_{\langle P_2 \rangle} = 0.9$ (open circles). (b) Evolution of D_e values with the contrast range $CR_{\langle P_2 \rangle}$ for bedding ($n_{\langle P_2 \rangle} = 5.5$; open diamonds) and random microstructures (crosses; see section 3.3.1 for details). In (a) and (b), the homogeneous microstructure is shown as orange square and diamond for $D_{e\overline{xy}}$ and D_{ez}, respectively. The simulated D_e values using the maps obtained from 2D-µXRD for the centrifuged IDP sample (Table 1) are also indicated in red solid circles. Four selected maps are shown on the right part of the figure in (a) and (b). In (a), the homogeneous organization is compared to the bedding microstructure with $CR_{\langle P_2 \rangle} = 0.3$ and $n_{\langle P_2 \rangle} = 4$, 8, and 16. In (b), the bedding microstructure at two $CR_{\langle P_2 \rangle}$ values (top) are compared to its corresponding random organization (bottom). (For interpretation of the references to colour in this figure legend, the reader is referred to the web version of this article.)

increase in $D_{e\overline{xy}}$ values; Fig. 5a). For the higher $\langle P_2 \rangle$ value (i.e., $\overline{\langle P_2 \rangle} = 0.52$), a similar variation in D_e values is observed compared to the homogeneous case as the CR_ε value increases.

The evolution of D_e values with CR_ε for bedding (with the number of porosity bedding $n_\varepsilon = 5.5$) and random patterns reveals very distinct features (Fig. 5b). For the bedding pattern, an increase in $D_{e\overline{xy}}$ and a decrease in D_{ez} is found to be progressive throughout the CR_ε range. This evolution can be explained by the bedding organization of low porosity pixels that act as a barrier to the diffusion of water along the z-direction. At the same time, the high-porosity beddings play the role of channels that enhance water diffusion in the $\overline{xy}$-direction. Consequently, the anisotropy in water diffusion (i.e., $D_{e\overline{xy}}/D_{ez}$) is strongly impacted by the CR_ε value for the bedding pattern. For $\overline{\langle P_2 \rangle} = 0$, this anisotropy ratio indeed increases from 0.0 to 3.6 for $CR_\varepsilon = 0.0$ and 0.7, respectively. In the case of $\overline{\langle P_2 \rangle} = 0.52$, this ratio increases from 2.2 to 11.0 within the same CR_ε range. The evolution of anisotropy in water diffusion due to the elongated porosity bedding is consistent with the findings of Robinet et al. (2012). These authors indeed showed that the elongated low-porous quartz or carbonate grains were responsible for the anisotropic features of water diffusion, even in the case of isotropic orientation of clay particles ($\langle P_2 \rangle = 0$).

For the random pattern and $\overline{\langle P_2 \rangle} = 0$, the decreasing evolution of D_{ez} and $D_{e\overline{xy}}$ is identical, and the lower D_e values are consistent with the increased amounts of low-porosity pixels that enhance the overall tortuosity in the sample. A similar situation occurs for random pattern at $\overline{\langle P_2 \rangle} = 0.52$, with a reduction of both D_{ez} and $D_{e\overline{xy}}$ values when increasing CR_ε values (Fig. 5b). However, it should be noted that the diffusion anisotropy ratio decreases for random pattern with evolution of CR_ε values from 0.0 to 0.7 (i.e., from $D_{e\overline{xy}}/D_{ez} = 2.2$ to 1.8, between $CR_\varepsilon = 0.0$ and 0.7, respectively). This can be attributed to the random spatial organization of low-porosity pixels, which moderates the influence of the orientation of clay particles on the overall water mobility.

To further evaluate the D_e evolution between the bedding and random patterns, an additional calculation was performed (Fig. 6). For the bedding pattern with $\overline{\langle P_2 \rangle} = 0.52$ and $CR_\varepsilon = 0.7$, the degree of randomness (R) was gradually increased to follow its impact on the D_e evolution (with $R = 0$ and $R = 1$ corresponding to the full bedding and full random patterns, respectively). As with generating the full random pattern, this was achieved by considering the bedding pattern and swapping the porosity values between two randomly chosen pixels. The

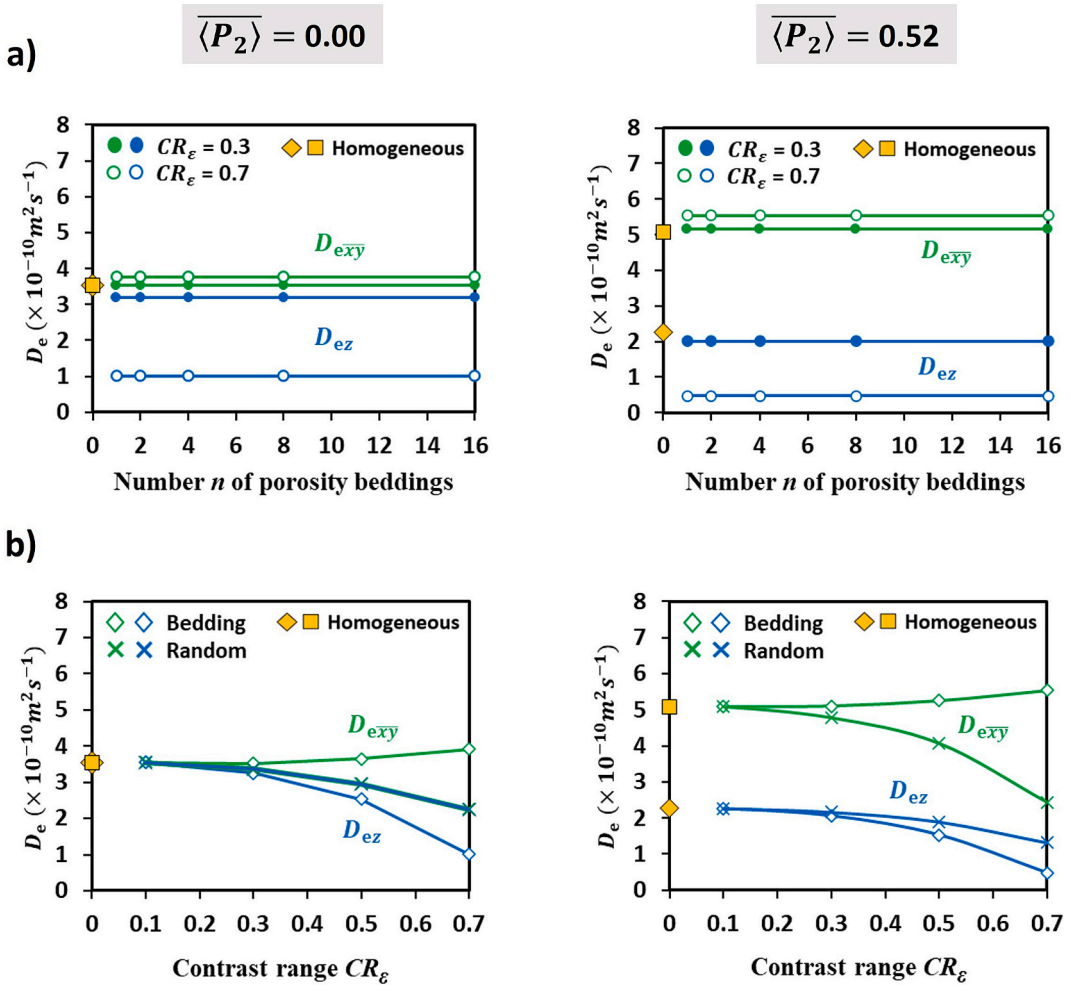


Fig. 5. Influence of the porosity microstructure on the calculated water effective diffusion coefficient (D_e) for $\overline{\langle P_2 \rangle} = 0.00$ (left) and $\overline{\langle P_2 \rangle} = 0.52$ (right). (a) Evolution of the D_e values with the number n of beddings for two contrast ranges, i.e., $CR_\varepsilon = 0.3$ (solid circles) and $CR_\varepsilon = 0.7$ (open circles). (b) Evolution of D_e values with the contrast range CR_ε for bedding ($n = 5.5$; open diamonds) and random microstructures (crosses; see section 3.3.2 for details). In (a) and (b), the homogeneous microstructure is shown as orange square and diamond for $D_{e\overline{xy}}$ and D_{ez}, respectively.

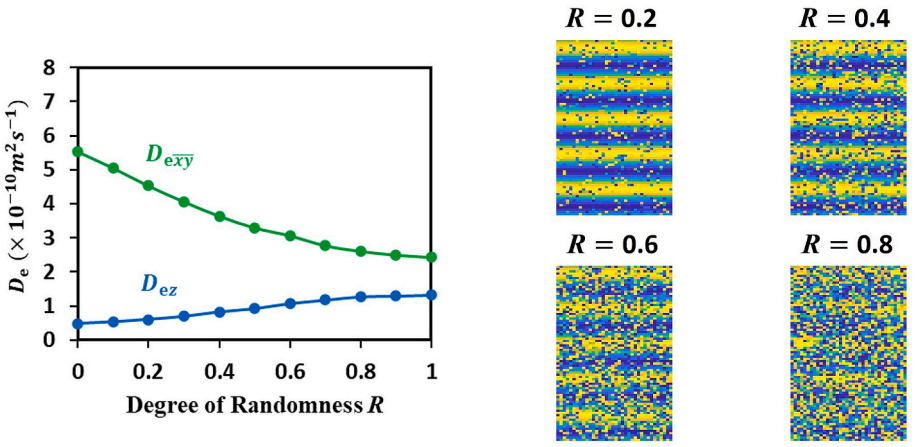


Fig. 6. Evolution of the water effective diffusion coefficient D_e in both the $\overline{xy}$- and z-directions as a function of randomness degree R, starting from the bedding pattern with $\bar{\varepsilon} = 0.38$, $\overline{\langle P_2 \rangle} = 0.52$, and $CR_\varepsilon = 0.7$ (Fig. 5b). Four selected maps are shown in the right part of the figure with $R = 0.2$, 0.4, 0.6, and 0.8.

degree of randomness R then corresponds to the relative proportion of swapped pixels in the map. Increasing the R value induces a progressive increase in D_{ez} and a decrease in $D_{e\overline{xy}}$ (Fig. 6).

The investigation of the influence of heterogeneity in ε and $\langle P_2 \rangle$ microstructure on the D_e values show the higher sensitivity of D_e towards ε than $\langle P_2 \rangle$. This can be interpreted based on the respective weights of these parameters in the extended Archie equations proposed by Ferrage et al. (2023) in Eqs. (8) and (9). The results also reveal that

the anisotropy in water diffusion can be significantly affected by the heterogeneity pattern of porosity (i.e., homogeneous, bedding, or random pattern) which can either intensify or moderate the diffusion anisotropy linked to the preferred orientation of clay particles.

4. Concluding remarks and perspectives

This study highlights the prominent role of porosity heterogeneity in pure clay samples on D_e values (Fig. 5) using very different theoretical and extreme heterogeneity patterns (i.e., homogeneous, bedding, and random). Indeed, both the frequency distribution of the pixel values and their organization pattern can lead to a significant variation of the D_e values and diffusion anisotropy ratios. This is especially the case when the microstructure displays a bedding pattern, for which the D_{ez} value can be reduced by a factor of up to 3 compared to the homogeneous pattern. The anisotropy ratio $D_{e\overline{xy}}/D_{ez}$ linked to the preferred orientation of clay particles (Ferrage et al., 2023) can be increased in the case of porosity bedding pattern, or reduced in the case of a random pattern. The number of beddings has no influence on the calculated D_e values, however.

The synchrotron 2D-μXRD technique is found to be a particularly useful technique to reveal the microstructure and spatial heterogeneity of ε, $\langle P_2 \rangle$, and Δ parameters (Fig. 2). The extraction of these maps allows for taking into account the actual microstructure of the sample in the calculation of water diffusion coefficients. Regarding the laboratory-made IDP samples (Table 1), the almost homogeneous porosity organization led to similar D_e values when comparing calculations based either on homogeneous (i.e., mean values for ε, $\langle P_2 \rangle$, and Δ parameters) or heterogeneous pattern (i.e., from experimental 2D-μXRD maps). This finding tends to validate the interpretation of water diffusion coefficients made so far based only on mean ε and $\langle P_2 \rangle$ values in laboratory-made samples (Dabat et al., 2020; Asaad et al., 2021; Ferrage et al., 2023).

Regarding the preferred orientation of clay particle, the heterogeneity in $\langle P_2 \rangle$ has only marginal effect on the water diffusion coefficients. All variations of the D_e values reported here (i.e., $< 10\%$; Fig. 4) indeed fall within the uncertainty limit of experimental measurements for pure clay systems (e.g., Glaus et al., 2010; Tertre et al., 2018; Asaad et al., 2021; Désert et al., 2025). However, it should be emphasized that the mean $\langle P_2 \rangle$ value remains a key parameter for the interpretation and prediction of water effective diffusion coefficients, in line with the work of Ferrage et al. (2023).

While the findings discussed in this study specifically pertain to pure clay media, they also offer fresh perspectives for polyphasic clay-rich systems, such as host rocks envisaged for nuclear waste disposal. Indeed, heterogeneous microstructures are systematically reported in these polyphasic rocks (Hemes et al., 2013; Pardoen et al., 2020; Yuan et al., 2022; Wüst et al., 2026). In this context, a perspective of this study is to extend the research to polyphasic materials and to take advantage of synchrotron 2D-μXRD to map the mineralogy of natural rocks. As far as the migration of cations and anions is concerned for these clay rocks, microstructural heterogeneity is also expected to play a role in their diffusion properties, in addition to the influence of electrostatic interactions occurring within the diffuse double layer located in the vicinity of the clay surfaces (Bourg and Tournassat, 2015; and references therein). The methodology used in the present study could then allow for a detailed investigation of the role of microstructure on the variability of water and solutes diffusion coefficients in clay-rich environments to improve the accuracy of predictions.

CRediT authorship contribution statement

Reza Aghlmand: Writing – review & editing, Writing – original draft, Visualization, Validation, Methodology, Investigation, Formal analysis, Data curation, Conceptualization. **Baptiste Dazas:** Writing – review & editing, Investigation, Data curation. **Ali Asaad:** Writing – review & editing, Investigation. **Christophe Tournassat:** Writing – review & editing, Software. **Fabien Hubert:** Writing – review & editing, Investigation. **Emmanuel Tertre:** Writing – review & editing, Investigation. **Eric Ferrage:** Writing – review & editing, Writing – original draft, Validation, Supervision, Project administration, Methodology, Funding acquisition, Conceptualization.

Declaration of competing interest

The authors declare that they have no known competing financial interests or personal relationships that could have appeared to influence the work reported in this paper.

Acknowledgements

The results presented here are part of the Ph.D. thesis of Reza Aghlmand, granted by the University of Poitiers, France. Part of the results were obtained from the "Environmental Mineralogy" platform at IC2MP from the "Experimental BioGeochemistry" network of the RéGEF National Infrastructure (fr-esr-fdr-ir-117). The authors acknowledge the Synchrotron SOLEIL (Saint-Aubin, France) for access to the CRISTAL beamline (Proposal No. 20200120-standard). The authors are grateful to the European Joint partnership EURAD 2 (WP "Rampec" – Grant Agreement N° 101166718) and the CNRS "défi Needs" interdisciplinary program (Project DARIUS) for the financial support of this study. The French government program "Investissements d'Avenir" (EUR INTREE, reference ANR-18-EURE-0010), the European Union (ERDF), and "Région Nouvelle-Aquitaine" are also acknowledged. C.T. acknowledges support from the U.S. Department of Energy, Office of Science, Office of Basic Energy Sciences, Chemical Sciences, Geosciences, and Biosciences Division, through its Geoscience program at LBNL under Contract No. DE-AC02-05CH11231. C.T. acknowledges a grant overseen by the French National Research Agency (ANR) as part of the "Investissements d'Avenir" Programme LabEx VOLTAIRE, 10-LABX-0100, and support from the CNRS International Research Project (IRP) "Reactive Transport Modeling into the Future".

Data availability

Data will be made available on request.

References

Altmann, S., Tournassat, C., Goutelard, F., Parneix, J.-C., Gimmi, T., Maes, N., 2012. Diffusion-driven transport in clayrock formations. Appl. Geochem. 27, 463–478. https://doi.org/10.1016/j.apgeochem.2011.09.015.

Appelo, C.A.J., Van Loon, L.R., Wersin, P., 2010. Multicomponent diffusion of a suite of tracers (HTO, Cl, Br, I, Na, Sr, Cs) in a single sample of Opalinus Clay. Geochim. Cosmochim. Acta 74, 1201–1219. https://doi.org/10.1016/j.gca.2009.11.013.

Asaad, A., 2021. Influence of Particles Organization and Dual Porosity on the Diffusion of Water and Solutes in Clayey Porous Media (Doctoral Dissertation). Université de Poitiers, Poitiers, France.

Asaad, A., Hubert, F., Ferrage, E., Dabat, T., Paineau, E., Porion, P., Savoye, S., Gregoire, B., Dazas, B., Delville, A., Tertre, E., 2021. Role of interlayer porosity and particle organization in the diffusion of water in swelling clays. Appl. Clay Sci. 207, 106089. https://doi.org/10.1016/j.clay.2021.106089.

Asaad, A., Hubert, F., Dazas, B., Razafitianamaharavo, A., Brunet, J., Glaus, M.A., Savoye, S., Ferrage, E., Tertre, E., 2022. A baseline study of mineralogical and morphological properties of different size fractions of illite du Puy. Appl. Clay Sci. 224, 106517. https://doi.org/10.1016/j.clay.2022.106517.

Bergaya, F., Theng, B., Lagaly, G., 2006. Handbook of Clay Science. Elsevier.

Bourg, I.C., Tournassat, C., 2015. Chapter 6 - Self-Diffusion of Water and Ions in Clay Barriers. In: Tournassat, C., Steefel, C.I., Bourg, I.C., Bergaya, F. (Eds.), Developments in Clay Science. Elsevier, pp. 189–226. https://doi.org/10.1016/B978-0-08-100027-4.00006-1.

Boving, T.B., Grathwohl, P., 2001. Tracer diffusion coefficients in sedimentary rocks: correlation to porosity and hydraulic conductivity. J. Contam. Hydrol. 53, 85–100. https://doi.org/10.1016/S0169-7722(01)00138-3.

Brusseau, M.L., 1993. The influence of solute size, pore water velocity, and intraparticle porosity on solute dispersion and transport in soil. Water Resour. Res. 29, 1071–1080. https://doi.org/10.1029/92WR02595.

Cho, W.J., Oscarson, D.W., Hahn, P.S., 1993. The measurement of apparent diffusion coefficients in compacted clays: an assessment of methods. Appl. Clay Sci. 8, 283–294. https://doi.org/10.1016/0169-1317(93)90009-P.

Dabat, T., Hubert, F., Paineau, E., Launois, P., Laforest, C., Grégoire, B., Dazas, B., Tertre, E., Delville, A., Ferrage, E., 2019. A general orientation distribution function for clay-rich media. Nat. Commun. 10. https://doi.org/10.1038/s41467-019-13401-0.

Dabat, T., Porion, P., Hubert, F., Paineau, E., Dazas, B., Grégoire, B., Tertre, E., Delville, A., Ferrage, E., 2020. Influence of preferred orientation of clay particles on the diffusion of water in kaolinite porous media at constant porosity. Appl. Clay Sci. 184, 105354. https://doi.org/10.1016/j.clay.2019.105354.

Dazas, B., Ferrage, E., Hubert, F., Gregoire, B., Fertey, P., Michot, L., 2026. LamelODF: a MATLAB-based toolbox for orientation distribution analysis and mapping of lamellar minerals for laboratory and synchrotron X-ray diffractometers. Appl. Crystallogr. 59. https://doi.org/10.1107/S1600576726000968.

Descostes, M., Blin, V., Grenut, B., Meier, P., Tevissen, E., 2004. HTO diffusion in Oxfordian limestone and Callovo-Oxfordian argillite formations. MRS Online Proc. Libr. 824, 402–407. https://doi.org/10.1557/PROC-824-CC8.29.

Désert, L., Savoye, S., Ferrage, E., Hubert, F., Henocq, P., Tournassat, C., Tertre, E., 2025. Effect of water saturation on the diffusive transport of water and solutes in compacted kaolinite, illite and vermiculite. Appl. Clay Sci. 276, 107928. https://doi.org/10.1016/j.clay.2025.107928.

Désert, L., Dazas, B., Mazurier, A., Michot, L.J., Tournassat, C., Tengattini, A., Henocq, P., Savoye, S., Tertre, E., Ferrage, E., 2026. Operando neutron tomography of the water through-diffusion front in illite under fully and partially water-saturated conditions. Appl. Clay Sci. 292, 108351. https://doi.org/10.1016/j.clay.2026.108351.

Ferrage, E., Hubert, F., Dabat, T., Asaad, A., Dazas, B., Grégoire, B., Savoye, S., Tertre, E., 2023. Anisotropy in particle orientation controls water diffusion in clay materials. Appl. Clay Sci. 244, 107117. https://doi.org/10.1016/j.clay.2023.107117.

Fox, P.M., Tournassat, C., Steefel, C., Nico, P.S., 2024. HTO and selenate diffusion through compacted Na-, Na–Ca-, and Ca-montmorillonite. Appl. Geochem. 170, 106090. https://doi.org/10.1016/j.apgeochem.2024.106090.

Gabis, V., 1958. Etude préliminaire des argiles oligocènes du Puy-en-Velay (Haute-Loire). Bull. Mineral. 81, 183–185.

Geoffroy, V., Dazas, B., Ferrage, E., Berenguer, F., Boissard, C., Michot, L.J., van Oort, F., Tertre, E., Hubert, F., 2022. Soil crusting: New insight from synchrotron 2D micro X-ray diffraction mapping of clay-particle orientation and mineralogy. Geoderma 428, 116096. https://doi.org/10.1016/j.geoderma.2022.116096.

Glaus, M.A., Rossé, R., Van Loon, L.R., Yaroshchuk, A.E., 2008. Tracer diffusion in sintered stainless steel filters: measurement of effective diffusion coefficients and implications for diffusion studies with compacted clays. Clays Clay Min. 56, 677–685. https://doi.org/10.1346/CCMN.2008.0560608.

Glaus, M.A., Frick, S., Rossé, R., Loon, L.R.V., 2010. Comparative study of tracer diffusion of HTO, 22Na+ and 36Cl− in compacted kaolinite, illite and montmorillonite. Geochim. Cosmochim. Acta 74, 1999–2010. https://doi.org/10.1016/j.gca.2010.01.010.

González Sánchez, F., Van Loon, L.R., Gimmi, T., Jakob, A., Glaus, M.A., Diamond, L.W., 2008. Self-diffusion of water and its dependence on temperature and ionic strength in highly compacted montmorillonite, illite and kaolinite. Appl. Geochem. 23, 3840–3851. https://doi.org/10.1016/j.apgeochem.2008.08.008.

Hemes, S., Desbois, G., Urai, J.L., De Craen, M., Honty, M., 2013. Homogeneity vs. Heterogeneity of Porosity in Boom Clay. In: Proceedings of the NEA Clay Club Workshop on Clay Characterisation from Nanoscopic to Microscopic Resolution. Karlsruhe (Germany), pp. 104–107.

Holz, M., Heil, S.R., Sacco, A., 2000. Temperature-dependent self-diffusion coefficients of water and six selected molecular liquids for calibration in accurate 1H NMR PFG measurements. Phys. Chem. Chem. Phys. 2 (20), 4740–4742. https://doi.org/10.1039/B005319H.

Hubbell, J.H., Seltzer, S.M., 1995. Tables of x-Ray Mass Attenuation Coefficients and Mass Energy-Absorption Coefficients 1 keV to 20 meV for Elements z = 1 to 92 and 48 Additional Substances of Dosimetric Interest. United States.

Huysmans, M., Dassargues, A., 2006. Stochastic analysis of the effect of spatial variability of diffusion parameters on radionuclide transport in a low permeability clay layer. Hydrogeol. J. 14, 1094–1106. https://doi.org/10.1007/s10040-006-0035-2.

Jacops, E., Aertsens, M., Maes, N., Bruggeman, C., Swennen, R., Krooss, B., Amann-Hildenbrand, A., Littke, R., 2017. The dependency of diffusion coefficients and geometric factor on the size of the diffusing molecule: observations for different clay-based materials. Geofluids 2017, 8652560. https://doi.org/10.1155/2017/8652560.

Kemper, W.D., van Schaik, J.C., 1966. Diffusion of salts in clay-water systems. Soil Sci. Soc. Am. J. 30, 534–540. https://doi.org/10.2136/sssaj1966.03615995003000050006x.

Koltermann, C.E., Gorelick, S.M., 1996. Heterogeneity in sedimentary deposits: a review of structure-imitating, process-imitating, and descriptive approaches. Water Resour. Res. 32, 2617–2658. https://doi.org/10.1029/96WR00025.

Liu, H.H., Bodvarsson, G.S., Zhang, G., 2004. Scale dependency of the effective matrix diffusion coefficient. Vadose Zone J. 3, 312–315. https://doi.org/10.2113/3.1.312.

Madsen, F.T., 1998. Clay mineralogical investigations related to nuclear waste disposal. Clay Miner. 33, 109–129. https://doi.org/10.1180/000985598545318.

Maes, N., Churakov, S., Glaus, M., Baeyens, B., Dähn, R., Grangeon, S., Charlet, L., Brandt, F., Poonoosamy, J., Hoving, A., Havlova, V., Fischer, C., Noseck, U., Britz, S., Siitari-Kauppi, M., Li, X., Fabritius, O., Missana, T., 2024. EURAD state-of-the-art report on the understanding of radionuclide retention and transport in clay and crystalline rocks. Front. Nucl. Eng. 3. https://doi.org/10.3389/fnuen.2024.1417827.

Martin, R.T., 1962. Adsorbed water on clay: a review. Clay Clay Miner. 28–70. https://doi.org/10.1016/B978-1-4831-9842-2.50007-9.

Mills, R., 1973. Self-diffusion in normal and heavy water in the range 1-45. Deg. J. Phys. Chem. 77, 685–688. https://doi.org/10.1021/j100624a025.

Oscarson, D.W., 1994. Surface diffusion: is it an important transport mechanism in compacted clays? Clays Clay Min. 42, 534–543. https://doi.org/10.1346/CCMN.1994.0420504.

Pardoen, B., Bésuelle, P., Dal Pont, S., Cosenza, P., Desrues, J., 2020. Accounting for small-scale heterogeneity and variability of clay rock in homogenised numerical micromechanical response and microcracking. Rock Mech. Rock. Eng. 53, 2727–2746. https://doi.org/10.1007/s00603-020-02066-7.

Poinssot, C., Baeyens, B., Bradbury, M.H., 1999. Experimental and modelling studies of caesium sorption on illite. Geochim. Cosmochim. Acta 63, 3217–3227. https://doi.org/10.1016/S0016-7037(99)00246-X.

Porion, P., Asaad, A., Dabat, T., Dazas, B., Delville, A., Ferrage, E., Hubert, F., Jiménez-Ruiz, M., Michot, L.J., Savoye, S., Tertre, E., 2021. Water and ion dynamics in confined media: a multi-scale study of the clay/water interface. Colloids Interfaces 5, 34. https://doi.org/10.3390/colloids5020034.

Pusch, R., 1992. Use of bentonite for isolation of radioactive waste products. Clay Miner. 27, 353–361. https://doi.org/10.1180/claymin.1992.027.3.08.

Pusch, R., 2006. Chapter 11.4 Clays and Nuclear Waste Management. In: Bergaya, F., Theng, B.K.G., Lagaly, G. (Eds.), Developments in Clay Science. Elsevier, pp. 703–716. https://doi.org/10.1016/S1572-4352(05)01023-8.

Robinet, J.-C., Sardini, P., Coelho, D., Parneix, J.-C., Prêt, D., Sammartino, S., Boller, E., Altmann, S., 2012. Effects of mineral distribution at mesoscopic scale on solute diffusion in a clay-rich rock: example of the Callovo-Oxfordian mudstone (Bure, France). Water Resour. Res. 48. https://doi.org/10.1029/2011WR011352.

Sarsenbayev, D., Tournassat, C., Steefel, C.I., Wainwright, H.M., 2025. Building confidence in models for complex barrier systems for radionuclides. Proc. Natl. Acad. Sci. U. S. A. 122, e2511885122. https://doi.org/10.1073/pnas.2511885122.

Schäfer, T., Claret, F., Bauer, A., Griffault, L., Ferrage, E., Lanson, B., 2003. Natural organic matter (NOM)-clay association and impact on Callovo Oxfordian clay stability in high alkaline solution: Spectromicroscopic evidence. Journal de Physique IV (Proceedings) 104, 413–416. https://doi.org/10.1051/jp4:20030111.

Steefel, C.I., Appelo, C.A.J., Arora, B., Jacques, D., Kalbacher, T., Kolditz, O., Lagneau, V., Lichtner, P.C., Mayer, K.U., Meeussen, J.C.L., Molins, S., Moulton, D., Shao, H., Šimůnek, J., Spycher, N., Yabusaki, S.B., Yeh, G.T., 2015. Reactive transport codes for subsurface environmental simulation. Comput. Geosci. 19, 445–478. https://doi.org/10.1007/s10596-014-9443-x.

Tertre, E., Savoye, S., Hubert, F., Prêt, D., Dabat, T., Ferrage, E., 2018. Diffusion of water through the dual-porosity swelling clay mineral vermiculite. Environ. Sci. Technol. 52, 1899–1907. https://doi.org/10.1021/acs.est.7b05343.

Tournassat, C., Steefel, C.I., 2021. Modeling diffusion processes in the presence of a diffuse layer at charged mineral surfaces: a benchmark exercise. Comput. Geosci. 25, 1319–1336. https://doi.org/10.1007/s10596-019-09845-4.

Tournassat, C., Steefel, C.I., Fox, P.M., Tinnacher, R.M., 2023. Resolving experimental biases in the interpretation of diffusion experiments with a user-friendly numerical reactive transport approach. Sci. Rep. 13. https://doi.org/10.1038/s41598-023-42260-5.

Tyagi, M., Gimmi, T., Churakov, S.V., 2013. Multi-scale micro-structure generation strategy for up-scaling transport in clays. Adv. Water Resour. 59, 181–195. https://doi.org/10.1016/j.advwatres.2013.06.002.

Van Laer, L., Aertsens, M., Maes, N., Van Loon, L.R., Glaus, M.A., Wüst, R.A.J., 2024. Diffusion of HTO, 36Cl and 22Na in the Mesozoic rocks of Northern Switzerland: III. Cross-lab comparison of diffusion measurements on argillaceous twin samples. Appl. Geochem. 160. https://doi.org/10.1016/j.apgeochem.2023.105840.

Van Loon, L.R., Soler, J.M., Jakob, A., Bradbury, M.H., 2003. Effect of confining pressure on the diffusion of HTO, 36Cl− and 125I− in a layered argillaceous rock (Opalinus Clay): diffusion perpendicular to the fabric. Appl. Geochem. 18, 1653–1662. https://doi.org/10.1016/S0883-2927(03)00047-7.

Van Loon, L.R., Soler, J.M., Müller, W., Bradbury, M.H., 2004. Anisotropic diffusion in layered argillaceous rocks: a case study with opalinus clay. Environ. Sci. Technol. 38, 5721–5728. https://doi.org/10.1021/es049937g.

Wang, C., Myshkin, V.F., Khan, V.A., Panamareva, A.N., 2022. A review of the migration of radioactive elements in clay minerals in the context of nuclear waste storage. J. Radioanal. Nucl. Chem. 331, 3401–3426. https://doi.org/10.1007/s10967-022-08394-y.

Wu, T., Dai, W., Xiao, G., Shu, F., Yao, J., Li, J., 2012. Influence of dry density on HTO diffusion in GMZ bentonite. J. Radioanal. Nucl. Chem. 292, 853–857. https://doi.org/10.1007/s10967-011-1523-y.

Wüst, R.A., Gimmi, T., Glaus, M.A., Van Loon, L.R., Wersin, P., Leupin, O., Wiechers, L., 2026. Constraining transport parameters for performance and safety assessments: bridging 30 years of Mont Terri in-situ diffusion experiments with laboratory-scale data of rock samples from deep drilling sites. Proceedings of the 43rd Mont Terri Technical meeting, 30th anniversary. April 29–30. Federal Office of Topography swisstopo, Porrentruy, Switzerland. https://doi.org/10.60695/swisstopo.mttm43.204.2026.

Yuan, T., Yang, Y., Ait-Mouheb, N., Deissmann, G., Fischer, C., Stumpf, T., Bosbach, D., 2022. A comparative study on heterogeneity of clay rocks using pore-scale diffusion simulations and experiments. J. Geophys. Res.: Solid Earth 127, e2022JB025428. https://doi.org/10.1029/2022JB025428.